

Supplementary Information for 3D-printed facet-attached microlenses for advanced photonic system assembly

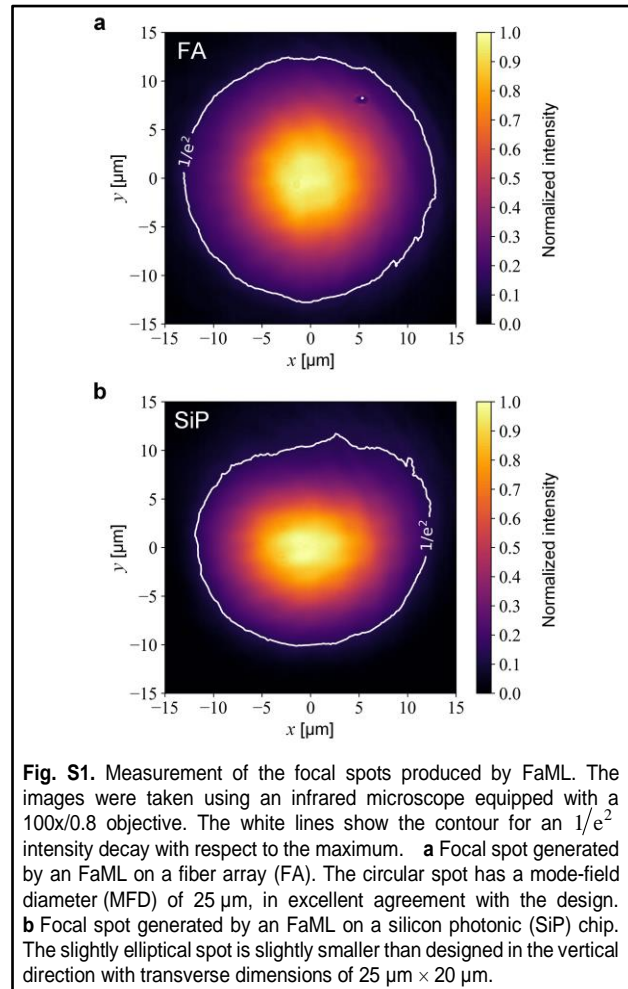
Yilin Xu^{1,2}, Pascal Maier^{1,2}, Mareike Trappen^{1,2}, Philipp-Immanuel Dietrich^{1,2,3}, Matthias Blaicher^{1,2}, Rokas Jutas¹, Achim Weber^{3,4}, Torben Kind⁴, Colin Dankwart⁴, Jens Stephan⁵, Andreas Steffan⁵, Amin Abbasi⁶, Padraic Morrissey⁷, Kamil Gradkowski⁷, Brian Kelly⁸, Peter O'Brien⁷, Wolfgang Freude¹ and Christian Koos^{1,2,3}

1. Spot-size measurement

To validate the design of the facet-attached microlenses (FaML), we first measure the associated spot sizes using an infrared microscope. Figure S1 shows the results for FaML on a fiber array (FA) and on a silicon photonic (SiP) chip as used in our first set of experiments, see Section “Facet-attached microlens on an SiP chip” of the main manuscript. In this case, the measurements were taken using a 100x/0.8 microscope objective. The focal position was determined by monitoring the brightness histogram of the image pixels at different axial positions and by identifying the position which produces maximum peak brightness. For the FaML on FA, we find a circular spot with a mode-field diameter (MFD) of 25 μm , in excellent agreement with the design. For the SiP chips, we fabricate an additional FaML on a separate channel (not shown in Fig. 2 of the main manuscript), for which the on-chip edge coupler (EC) is directly connected to a grating coupler (GC) to facilitate in-coupling of light. We find a slightly elliptical spot, which is a bit smaller than designed in the vertical direction, with transverse dimensions of 25 $\mu\text{m} \times 20 \mu\text{m}$. Note that this slight mode-field mismatch has only minor impact on the coupling efficiency and the alignment tolerances, see Section “Facet-attached microlens on an SiP chip” in the main manuscript.

2. Alignment of Gaussian beams

Usually, the facets of micro-optic components have small light-emitting or accepting areas and correspondingly big beam divergence angles. This allows a large rotational



Correspondence: Yilin Xu (yilin.xu@kit.edu) or

Christian Koos (christian.koos@kit.edu)

¹Institute of Photonics and Quantum Electronics (IPQ), Karlsruhe Institute of Technology (KIT), Engesserstr. 5, 76131 Karlsruhe, Germany

²Institute of Microstructure Technology (IMT), KIT, Hermann-von-Helmholtz-Platz 1, 76344 Eggenstein-Leopoldshafen, Germany

³Vanguard Automation GmbH, Gablonzerstr. 10, 76185 Karlsruhe, Germany

⁴ficonTEC Service GmbH, Im Finigen 3, 28832 Achim, Germany

⁵Il-VI Inc., Reuchlinstraße 10/11, 10553 Berlin, Germany

⁶Photonics Research Group, Ghent University – imec, Technologiepark-Zwijnaarde 126, B-9052 Gent, Belgium

⁷Tyndall National Institute, T12 R5CP Cork, Ireland

⁸Eblana Photonics Ltd., West Pier Business Campus, 3 Old Dunleary Rd, Dún Laoghaire, Dublin, A96 A621, Ireland

misalignment, but a low translational offset only. Our experiments demonstrate that assembly processes can benefit from reducing the divergence and simultaneously expanding the transverse mode-field dimensions by means of facet-attached microlenses (FaML). Our results shown in the main manuscript rely on suitable FaML designs which consider practical limitations such as tolerances of the fabrication and the assembly processes. These designs are based on quantitative models¹ for the translational lateral and for the rotational alignment tolerances of Gaussian beams, which we explain in the following. These models are also essential for benchmarking our experimental results.

As a model configuration, we consider a free-space connection from a single-mode source to a single-mode sink. We assume Gaussian beams which implies the limitations of paraxial approximation. For simplicity and according to the practical situation, we assume rotationally symmetric beams. Note, however, that the derivations can be extended to elliptic stigmatic beams¹. Without loss of generality, the principal beam-propagation direction is z with $z = 0$ in the beam waist. We further use a “positive” time dependence of the form $\exp(j(\omega t - kz))$ for a wave propagating at angular frequency ω in positive z -direction with a propagation constant k . The only remaining beam parameter is the waist radius w_0 . In addition, the beam is characterized by the Rayleigh distance z_R , the z -dependent beam radius $w(z)$ defined by a $1/e^2$ decay of the intensity compared to it on-axis maximum, the asymptotic divergence angle θ_{div} , the z -dependent phase-front curvature $\kappa(z)$, and the Gouy phase $\zeta(z)$,

$$z_R = \frac{k w_0^2}{2}, \quad (\text{S1})$$

$$w(z) = w_0 \sqrt{1 + \left(\frac{z}{z_R}\right)^2}, \quad (\text{S2})$$

$$\theta_{\text{div}} \approx \tan \theta_{\text{div}} = \frac{2}{k w_0}, \quad (\text{S3})$$

$$\kappa(z) = \frac{z}{z^2 + z_R^2}, \quad (\text{S4})$$

$$\zeta(z) = \arctan\left(\frac{z}{z_R}\right). \quad (\text{S5})$$

With these parameters, the complex amplitude $\psi(r, z)$ of the scalar field can be written in cylindrical coordinates (r, z) ,

$$\psi(r, z) = \sqrt{\frac{2}{\pi}} \frac{1}{w(z)} e^{-r^2/w^2(z)} e^{-jk r^2 \kappa(z)/2} e^{-j(kz - \zeta(z))}. \quad (\text{S6})$$

The normalization is chosen such that

$$2\pi \int_0^\infty |\psi(r, z)|^2 r dr = 1. \quad (\text{S7})$$

Our model configuration consists of two Gaussian beams, see Fig. S2. The beam $\psi(r, z)$ emitted from the source is described by Eq. (S6) and Eq. (S7), having its waist located at the origin of the coordinate system, black contours in Fig. S2a. It is coupled to a second Gaussian beam $\bar{\psi}(\bar{r}, \bar{z})$ accepted by the sink, indicated by blue contours in Fig. S2a. This beam is described with respect to a second coordinate system (\bar{r}, \bar{z}) that may be rotated with respect to the coordinate system (r, z) of the first beam by an angle θ , see Fig. S2c. The second beam is also described by Eq. (S6) and Eq. (S7), where all quantities but ω and k carry an overbar. We choose an arbitrary reference plane S_{ref} in free space, where the overlap integral is calculated. In addition to a mode-field radius

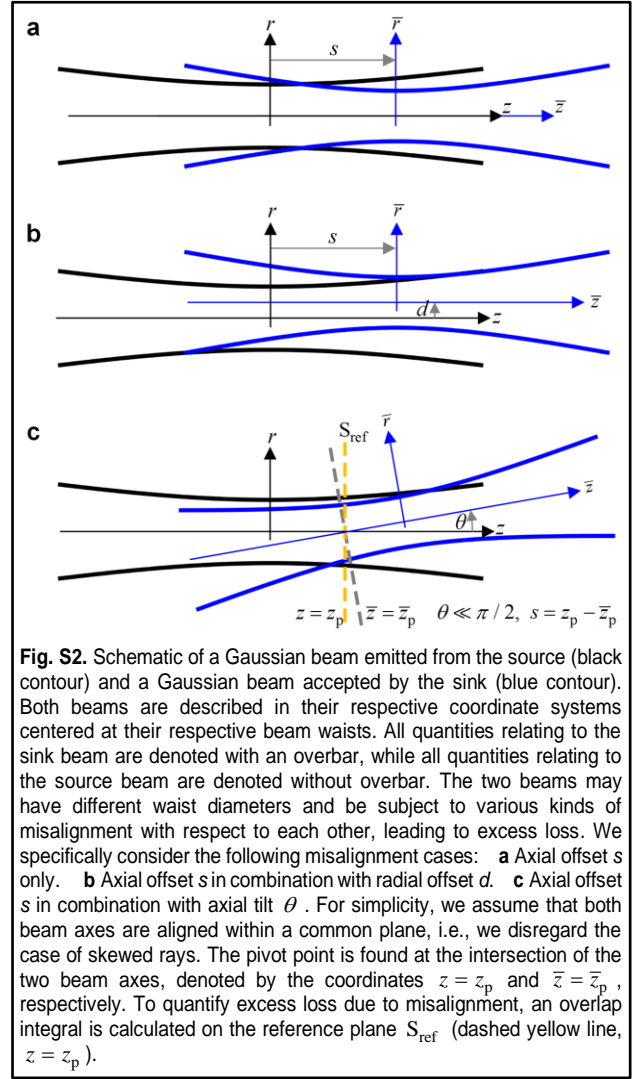


Fig. S2. Schematic of a Gaussian beam emitted from the source (black contour) and a Gaussian beam accepted by the sink (blue contour). Both beams are described in their respective coordinate systems centered at their respective beam waists. All quantities relating to the sink beam are denoted with an overbar, while all quantities relating to the source beam are denoted without overbar. The two beams may have different waist diameters and be subject to various kinds of misalignment with respect to each other, leading to excess loss. We specifically consider the following misalignment cases: **a** Axial offset s only. **b** Axial offset s in combination with radial offset d . **c** Axial offset s in combination with axial tilt θ . For simplicity, we assume that both beam axes are aligned within a common plane, i.e., we disregard the case of skewed rays. The pivot point is found at the intersection of the two beam axes, denoted by the coordinates $z = z_p$ and $\bar{z} = \bar{z}_p$, respectively. To quantify excess loss due to misalignment, an overlap integral is calculated on the reference plane S_{ref} (dashed yellow line, $z = z_p$).

mismatch we specifically consider three types of misalignment, Fig. S2: Axial offset by a distance s , Fig. S2a, axial offset s in combination with radial offset d , Fig. S2b, and axial offset s in combination with axial tilt θ , Fig. S2c. In the following, we discuss the different cases and quantify the dependence of the coupling loss on the respective parameters s , d , and θ . For simplicity, we first analyze the case of combined axial offset and axial tilt, Fig. S2c, and use the result to derive the relations of the other cases.

2.1 Axial offset and axial tilt

The combined axial and angular misalignment of the sink beam (blue) with respect to the source beam (black), Fig. S2c, can be constructed in three steps: Starting from a perfect alignment where the coordinate systems of both beams coincide, the sink beam is first shifted by a distance z_p along the still collinear beam axes. The sink beam is then rotated by a small angle θ about its beam waist, followed by another translation $-\bar{z}_p$ in the rotated coordinate system. The pivot point of combined translation and rotation mapping is finally found at the intersection of the two beam axes, i.e., at a coordinate $z = z_p$ in the coordinate system of the source

beam, and at a coordinate $\bar{z} = \bar{z}_p$ in the coordinate system of the sink beam. We further introduce the signed axial offset $s = z_p - \bar{z}_p$ between the beam waists. Note that both beam axes aligned along the z - and \bar{z} -direction still lie within a common plane, i.e., we disregard the case of skewed rays. Within this plane of the rotation, we can hence formulate the transformation between the coordinate systems of both beams and the associated approximations for small angles θ as

$$\begin{aligned}\bar{z} &= (z - z_p)\cos\theta + r\sin\theta + \bar{z}_p \approx z - s + r\theta \\ \bar{r} &= -(z - z_p)\sin\theta + r\cos\theta \approx -(z - z_p)\theta + r\end{aligned}\quad (\text{S8})$$

As reference plane S_{ref} for performing the overlap integral that quantifies the coupling efficiency, we choose the plane $z = z_p$ parallel to the (x, y) -plane, yellow dashed line in Fig. S2c, which contains the pivot point of the rotation. Note, however, that this choice is arbitrary – any other transverse reference plane should lead to the same result. For small angles θ , this plane can be described in the coordinate system of the sink beam by using Eq. (S8),

$$\bar{z} \approx z_p - s + r\theta = \bar{z}_p + r\theta, \quad \bar{r} \approx r, \quad (\text{S9})$$

where $s = z_p - \bar{z}_p$. We further assume a small divergence angle of the sink beam such that the sink beam radius $\bar{w}(\bar{z}_p)$ in plane $\bar{z} = \bar{z}_p$ corresponds approximately to the radius $\bar{w}(\bar{z}_p)\cos\theta \approx \bar{w}(\bar{z}_p)$ in plane $z = z_p$. The same argument holds true for the \bar{z} -dependent Gouy phase, which is approximated by $\zeta(\bar{z}_p)$ in the relevant part of the reference plane $z = z_p$, independent of r . The complex field of the sink beam in the reference plane can hence be approximated by

$$\bar{\psi}(\bar{r} \approx r, \bar{z} \approx \bar{z}_p + r\theta) \approx \bar{\psi}(r, \bar{z}_p)e^{-jkr\theta}. \quad (\text{S10})$$

Under these assumptions, the overlap integral for the power transmission T_R in the reference plane S_{ref} can be written as

$$T_R = \left| 2\pi \int_0^\infty \psi^*(r, z_p) \bar{\psi}(r, \bar{z}_p) e^{-jkr\theta} r dr \right|^2. \quad (\text{S11})$$

Using Eqs. (S1), (S2), (S4), and (S6) leads, after some modifications¹, to a simplified expression for the power transmission,

$$T_R = \tau_a^2(s) e^{-(\theta/\theta_e)^2}, \quad s = z_p - \bar{z}_p, \quad (\text{S12})$$

where $\tau_a(s)$ describes the dependence of the excess loss on a pure axial offset s ,

$$\tau_a(s) = \frac{2}{\sqrt{\left(\frac{w_0}{\bar{w}_0} + \frac{\bar{w}_0}{w_0}\right)^2 + \left(\frac{2}{k w_0 \bar{w}_0}\right)^2 s^2}}, \quad (\text{S13})$$

and where θ_e quantifies the $1/e^2$ rotational alignment tolerance for a given axial offset s and positions z_p and \bar{z}_p ,

$$\theta_e = \frac{2\sqrt{2}}{k\tau_a(s)\sqrt{\bar{w}^2(\bar{z}_p) + w^2(z_p)}}. \quad (\text{S14})$$

The local spot-size radii $w(z_p)$ and $\bar{w}(\bar{z}_p)$ in Eq. (S14) are given according to Eq. (S2). The $1/e^2$ rotational alignment tolerance θ_e assumes its maximum value¹ $\theta_{e,\text{max}}$ if the relation

$$\frac{z_p}{w^2(z_p)} + \frac{\bar{z}_p}{\bar{w}^2(\bar{z}_p)} = 0, \quad (\text{S15})$$

is fulfilled, where

$$\theta_{e,\text{max}} = \frac{\sqrt{2}\sqrt{1/w_0^2 + 1/\bar{w}_0^2}}{k}. \quad (\text{S16})$$

Note that $\theta_{e,\text{max}}$ does not depend on the waist separation s , but the transmission $T_R \leq 1$ according to Eq. (S12) does and is maximum for $s = 0$, i.e., if the positions $z = 0$ and $\bar{z} = 0$ coincide. In the following, we specialize the relations Eq. (S12) – (S14) to axial tilt only ($s = 0$), and to axial offset only ($\theta = 0$).

2.2 Axial tilt only

A simplified expression for T_R results when considering the case without any mode-field mismatch ($w_0 = \bar{w}_0$) and without axial offset ($s = 0$). In this case, the $1/e^2$ rotational alignment tolerance $\theta_e = 2/(kw_0)$ corresponds to the (common) divergence angle of both beams, and the power transmission T_R simplifies to

$$T_R = e^{-(\theta/\theta_{\text{div}})^2}, \quad \theta_{\text{div}} = \frac{2}{kw_0}. \quad (\text{S17})$$

2.3 Axial offset only

The special case of an axial offset only, Fig. S2a, is described by setting $\theta = 0$ in Eq. (S12). The power transmission T_a for an axial offset s is thus

$$T_a = \tau_a^2(s), \quad (\text{S18})$$

where $\tau_a(s)$ is given by Eq. (S13). For perfect axial alignment ($s = 0$) and a mode-field-diameter mismatch only, we find

$$\tau_a(0) = \frac{2}{\bar{w}_0/w_0 + w_0/\bar{w}_0}. \quad (\text{S19})$$

If the mode-fields are matched, $w_0 = \bar{w}_0$, an axial

misalignment $s \neq 0$ leads to

$$\tau_a(s)|_{w_0=\bar{w}_0} = \frac{1}{\sqrt{1+s^2/(k^2w_0^4)}} = \frac{2}{\sqrt{4+(s/z_R)^2}}. \quad (\text{S20})$$

An axial shift of approximately one Rayleigh distance $s = z_R$ hence results in a misalignment loss of approximately 1 dB.

2.4 Combination of axial offset and lateral offset

Finally, we discuss the combination of an axial offset s and a lateral offset d , Fig. S2b. The expression for the associated power transmission T_L is derived from the previously discussed case of a combined axial offset and axial tilt, Eqs. (S12)...(S14). To this end and for the depicted case in Fig. S2c, we consider the limit¹

$$z_p \rightarrow -\infty, \quad \bar{z}_p = z_p - s \rightarrow -\infty \quad (\text{S21})$$

along with an infinitesimal rotation

$$\theta = d/|z_p|. \quad (\text{S22})$$

According to Eqs. (S1) and (S2) we then find

$$w(z_p) \rightarrow w_0 \frac{|z_p|}{z_R} = \frac{2|z_p|}{kw_0}, \quad \bar{w}(\bar{z}_p) \rightarrow \frac{2|z_p-s|}{k\bar{w}_0} \rightarrow \frac{2|z_p|}{k\bar{w}_0}. \quad (\text{S23})$$

Inserting Eqs. (S22) and (S23) into Eqs. (S12) and (S14) leads to the expression for the power transmission T_L ,

$$T_L = \tau_a^2(s) e^{-(d/d_c)^2}, \quad (\text{S24})$$

with

$$d_c = \frac{1}{\tau_a(s)} \sqrt{\frac{2}{1/w_0^2 + 1/\bar{w}_0^2}}. \quad (\text{S25})$$

2.5 Lateral offset only

We further give the expression for the simplified case of a lateral offset only ($s = 0$), without any mode-field mismatch ($w_0 = \bar{w}_0$). The power transmission T_L is then found using Eqs. (S24) and (S25),

$$T_L = e^{-(d/w_0)^2}. \quad (\text{S26})$$

From Eq. (S26), we find that a lateral shift of

$$d_{\text{1dB}} = \sqrt{\frac{1}{10 \log_{10} e}} \times w_0 \approx 0.48 \times w_0 \quad (\text{S27})$$

leads to a misalignment excess loss of 1 dB. This lateral shift is depicted by red dashed circles in Figs. 3a, 6c and 9b of the main manuscript, in excellent agreement with experimentally measured data for Figs. 3a and 6c, and in reasonable

agreement with experimentally measured data for the much more complex FaML assembly in Fig. 9b. The smallest MFD used in our experiments amounts to $25 \mu\text{m}$ ($w_0 = 12.5 \mu\text{m}$). In this case, a lateral shift of $d = 1 \mu\text{m}$, e.g. due to irregularities in the spacing of the fibers within the fiber array (FA), only leads to an excess loss of 0.03 dB according to Eq. (S26), which is fully negligible.

2.6 Measurement of rotational tolerances

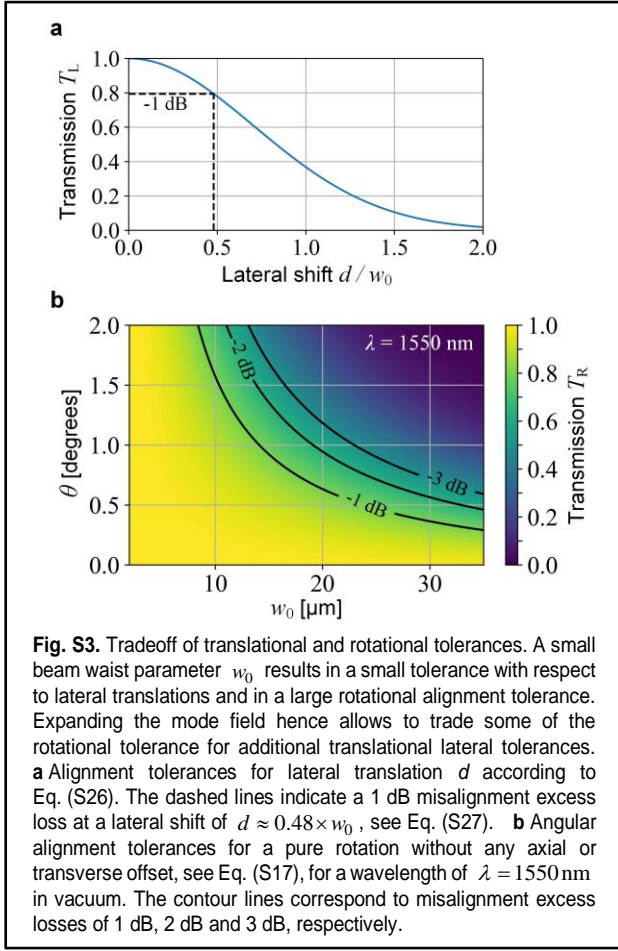
When experimentally measuring the angular alignment tolerance, the pivot point of the rotation is usually not precisely known. As a consequence, any rotation of the positioning stage has to be followed by a set of translations that compensate for the unwanted movement of the point $z = z_p$ or $\bar{z} = \bar{z}_p$ that is assumed to be the center of the rotation considered in Sections 2.1 and 2.2. These translations are performed as to maximize the coupling between the two beams without changing their angular orientation, thus leading to a configuration in which the center points of the two beam waists, marked by the points $z = 0$ and $\bar{z} = 0$ on the two beam axes, coincide, see discussion after Eq. (S16) above. The measurement procedure therefore effectively corresponds to a rotation around the pivot point for $s = 0$. In this case, $z_p = \bar{z}_p = 0$, such that Eq. (S15) is fulfilled. The extracted $1/e^2$ angular alignment tolerance hence corresponds to the maximum achievable value $\theta_{e,\text{max}}$ according to Eq. (S16), and according to Eq. (S17) it is further equal to the common divergence angle θ_{div} if there is no mode-field mismatch ($w_0 = \bar{w}_0$). This measurement procedure is used to obtain the experimental data of rotational alignment tolerances in Figs. 3b, 6e and 9c of the main manuscript, and the results are then fit by Eq. (S17) with the common beam-waist radius w_0 as a free parameter, from which the $1/e^2$ rotational alignment tolerance $\theta_{e,\text{max}} = \theta_{\text{div}}$ or the corresponding 1 dB tolerances are extracted.

2.7 Tradeoff of translational and rotational tolerances

For visualizing the aforementioned fundamental tradeoff between translational and rotational tolerances, Fig. S3, we consider the simplified case of a circularly symmetric beam without mode-field mismatch and without axial misalignment. The misalignment-dependent power transmission is thus calculated according to Eq. (S26) and Eq. (S17) for a translational lateral and for a rotational misalignment, respectively. A small beam waist parameter w_0 results in a small tolerable lateral shift d , Fig. S3a, but allows a large misalignment angle θ , Fig. S3b. Expanding the mode field increases the translational lateral tolerance, but decreases the rotational one.

2.8 Tolerance analysis for passive alignment

To arrive at easy-to-handle design guidelines for passively assembled FaML-based optical systems, we estimate the impact of positioning uncertainties on the excess coupling loss. The underlying passive assembly processes rely on aligning two components to each other by first fixing one



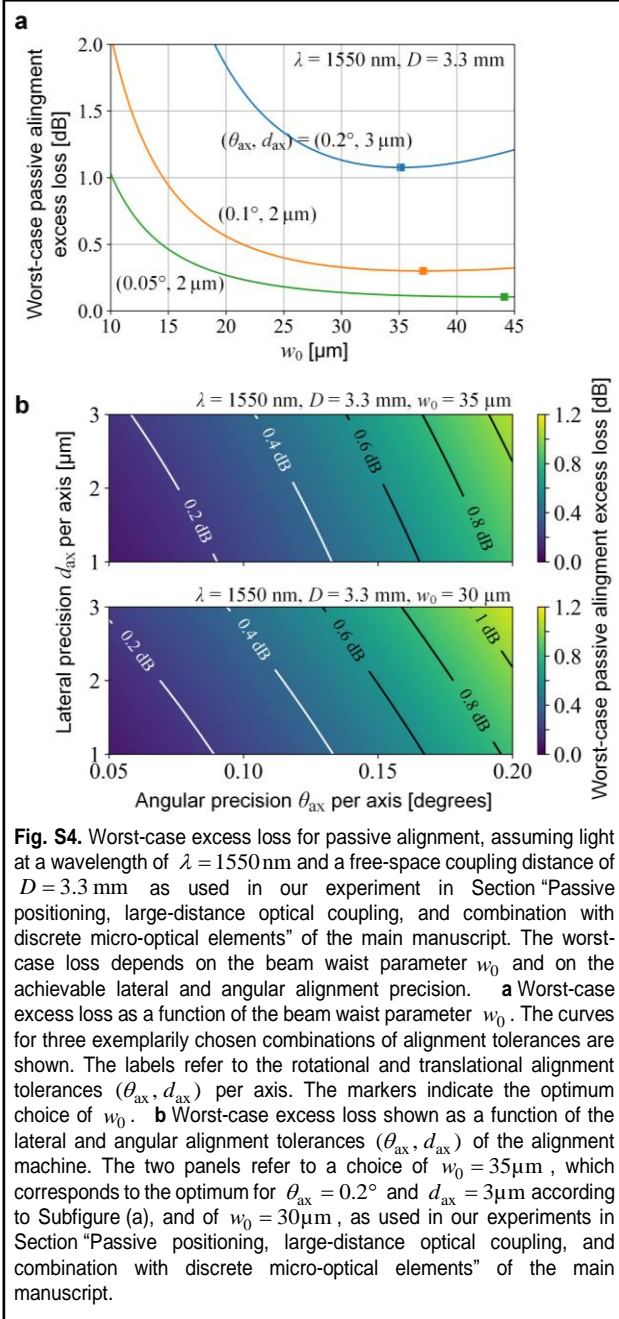
component in place and by aligning the second one based on measurements of positions and orientations. For the expanded beam, we may safely assume that slight axial misalignments do not play a significant role such that we only need to consider angular measurement error θ and an independent measurement error d of the lateral position, both of which result in a corresponding combined angular and lateral misalignment. We could represent this combined misalignment as a single axial tilt with a certain pivot point and calculate the net effect according to Eqs. (S12) – (S14). This is however complicated, and we instead use an approximation, where we consider the combined misalignment as the result of a rotation of one beam by an angle θ about a common beam waist, followed by a lateral shift by a distance d . We further assume that the losses of these two operations can be independently calculated according to Eq. (S17) and Eq. (S26), respectively, and that the corresponding power transmission factors can be simply multiplied to obtain the final power transmission factor of the overall configuration. We further consider a free-space coupling distance D and we assume a symmetric configuration, where the beam waists lie in the middle of the free-space distance. An angular misalignment θ of the second component would then lead to an additional lateral shift (pointing error) of the corresponding beam by $(D/2)\tan\theta$ in the plane of the common beam waists, where

we evaluate the overlap integral. The worst-case lateral shift d_{\max} to account for with Eq. (S26) is hence

$$d_{\max} = \left| \frac{D}{2} \tan\theta \right| + |d|, \quad (\text{S28})$$

where we have assumed that the induced lateral shift and the independent measurement error of the lateral position lead to a misalignment in the same direction. In the following, we consider a given free-space distance D and given precisions θ_{ax} and d_{ax} per rotational axis and per translational axis of the alignment machine, respectively. The rotation-independent lateral shift d within Eq. (S28) is hence $d = \sqrt{2}d_{\text{ax}}$ in the worst case, where we again assume that slight axial misalignments do not play a significant role such that only the misalignment along the two transverse directions contributes to the excess loss. Likewise, for small angles, we consider $\theta \approx \sqrt{2}\theta_{\text{ax}}$ in Eqs. (S28) and (S17), since a rotation about approximately collinear beam axes does not matter for a single free-space connection and rotationally symmetric beams. Note, however, that rotations about approximately collinear beam axes do play a role in case of assembly of device arrays with multiple free-space connections. In this case, the associated loss can be easily estimated based on Eq. (S26) and is usually not a limiting factor for chip-scale waveguide separations and typical FaML-generated free-space beam diameters of, e.g., $25 \mu\text{m}$ or larger. Under these premises there exists an optimum beam-waist radius w_0 , which yields the lowest reliably achievable loss, see Fig. S4a: For a very small waist radius w_0 , the expected total loss will be dominated by the worst-case lateral shift, Eqs. (S28) and (S26), while for a very large waist parameter, the expected total loss will be dominated by the rotation around the common beam waist and the corresponding inclination of the associated phase fronts, Eq. (S17). Alternatively, one can use Eq. (S28) in combination with Eqs. (S17) and (S26) to estimate the worst-case coupling loss for given rotational and translational tolerances of the machine-vision-based alignment system, see Fig. 4b.

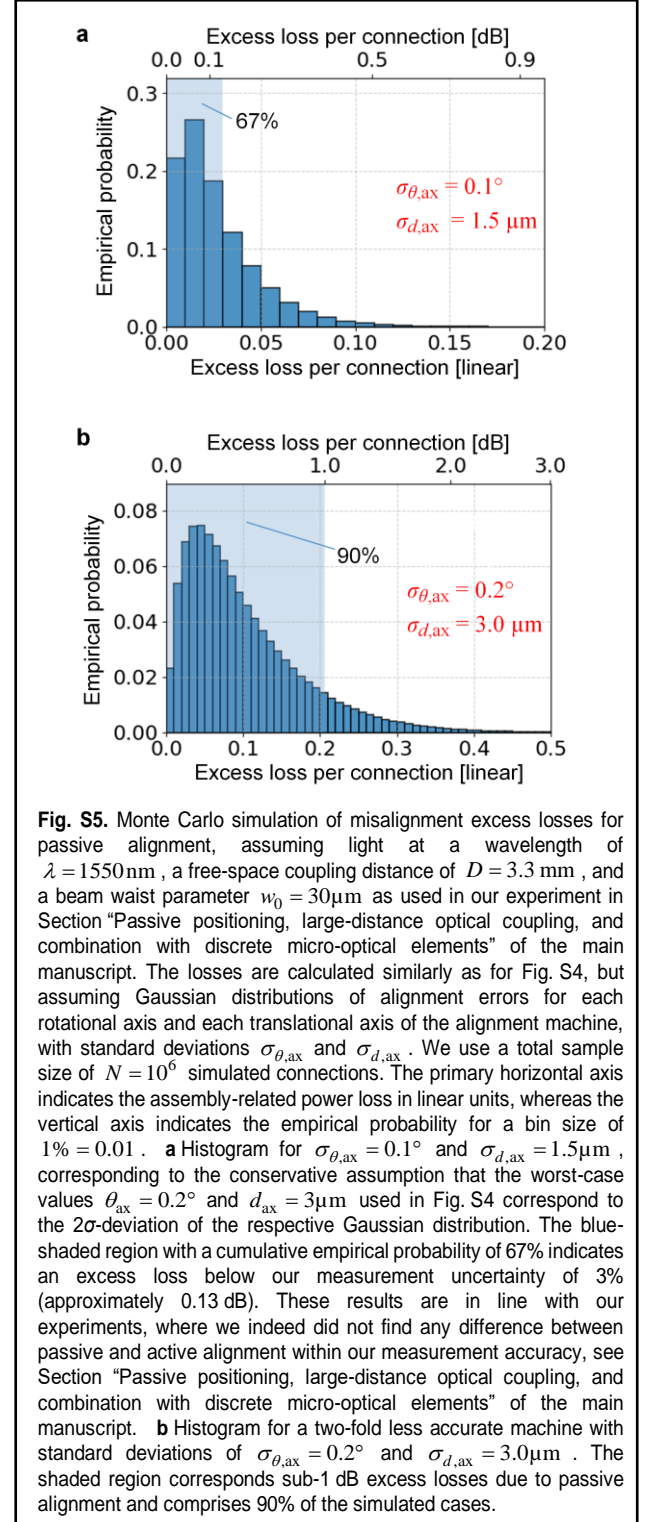
In our passive assembly experiment over a large distance of 3.3 mm , see Section “Passive positioning, large-distance optical coupling, and combination with discrete micro-optical elements” of the main manuscript, we used lenses which produce a beam diameter of $2w_0 = 60 \mu\text{m}$ (beam radius $w_0 = 30 \mu\text{m}$). Note that, for an initial conservative estimate of $\theta_{\text{ax}} = 0.2^\circ$ for each rotation axis and $d_{\text{ax}} = 3 \mu\text{m}$ for each translation axis, a beam diameter of $2w_0 \approx 70 \mu\text{m}$ would have been ideal, see Fig. S4a. However, we found this beam diameter difficult to reach with only two refractive surfaces under the limitations of the lithography system regarding the maximum structure size. We thus performed our experiments with a slightly smaller beam diameter of $60 \mu\text{m}$, which does not severely limit our performance, see Fig. S4b. Given the fact that our passive alignment prior to gluing leads to an angular position that is practically identical to the actively optimized position within the measurement accuracy, see



Section “Passive positioning, large-distance optical coupling, and combination with discrete micro-optical elements” of the main manuscript, we believe that even larger beam diameters could have been used. This would also have decreased the variations of the coupling losses obtained for different path lengths in our experiment including the polarization beam splitter, see Eq. (S20) and Section “Passive positioning, large-distance optical coupling, and combination with discrete micro-optical elements” of the main manuscript.

2.9 Monte-Carlo simulations of coupling losses

While Fig. S4 depicts the worst-case excess loss for passive assembly, the statistics of assembly losses is also an important factor, in particular when it comes to industrial exploitation of



the processes. We therefore extend the worst-case analysis of Supplementary Section 2.8 by conducting Monte Carlo simulations, in which we perform similar calculation steps as for Fig. S4, but assume a Gaussian distribution of alignment errors for each rotational axis and each translational axis of the assembly machine with standard deviations $\sigma_{\theta_{ax}}$ and $\sigma_{d_{ax}}$, respectively. For each realization, we calculate the lateral shift of the beam waists with respect to one another and

then use the relations given in Eq. (S17) and Eq. (S26) to estimate the associated losses – rather than just taking the worst-case shift as in Eq. S(28). Fig. S5 depicts the histograms of the resulting misalignment excess losses for a total sample size of $N=10^6$ simulated connections. The primary horizontal axis indicates the assembly-related excess power loss in linear units, and the vertical axis indicates the empirical probability for a bin size of $1\% = 0.01$, i.e., the share of resulting losses that are within the respective bin. In the calculations, the beam waist parameter and the free-space coupling distance are set to $w_0 = 30\mu\text{m}$ and $D = 3.3\text{mm}$, respectively, corresponding to the values used in our experiments, see Section “Passive positioning, large-distance optical coupling, and combination with discrete micro-optical elements” of the main manuscript. The calculations in Fig. S5a are performed with the conservative assumption that the estimated worst-case values $\theta_{\text{ax}} = 0.2^\circ$ and $d_{\text{ax}} = 3\mu\text{m}$ of Section 2.8 correspond the 2σ -deviations of the underlying Gaussian distributions, i.e., $\sigma_{\theta,\text{ax}} = 0.1^\circ$ and $\sigma_{d,\text{ax}} = 1.5\mu\text{m}$. The blue-shaded region in Fig. S5a with a cumulative empirical probability of 67% indicates an excess loss below our measurement uncertainty of 3% (approximately 0.13 dB). This result is in line with our experiments, where we indeed did not find any difference between passive and active alignment within our measurement accuracy, see Section “Passive positioning, large-distance optical coupling, and combination with discrete micro-optical elements” of the main manuscript. We also show that in case of a significantly less accurate machine with two-fold increased alignment tolerances of $\sigma_{\theta,\text{ax}} = 0.2^\circ$ and $\sigma_{d,\text{ax}} = 3.0\mu\text{m}$, Fig. S5b, the excess losses due to passive alignment are still below 1 dB in 90% of the cases. These results confirm the robustness of FaML-based assembly processes and their potential for high-yield production.

3. Assembly machine and passive alignment process

All assemblies have been built using a custom semi-automated assembly machine (ficonTEC Service GmbH) that relies on industry-standard machine vision techniques, see Fig. S6. The submount of the assembly is held in place at the assembly zone using a vacuum chuck. Components such as optical chips or fiber arrays are mounted using a six-axis positioner (right side) that is equipped with either a gripper or vacuum pick-up-tool (PUT). The positions and orientations of components after pick-up and/or mounting are measured using a top view (TV) camera and a chromatic confocal distance sensor², both mounted on a three-axis positioner (left side), as well as another fixed bottom-view (BV) camera. In a typical assembly workflow, parts are first picked up from the tray, inspected over the BV camera if necessary, and moved over to the assembly zone for final alignment and fixing. In our experiments, we demonstrate a passively aligned assembly with a large coupling distance, see Section “Passive positioning, large-distance optical coupling, and combination with discrete micro-optical elements” of the main manuscript, where we couple a fiber array (FA) to a photo diode

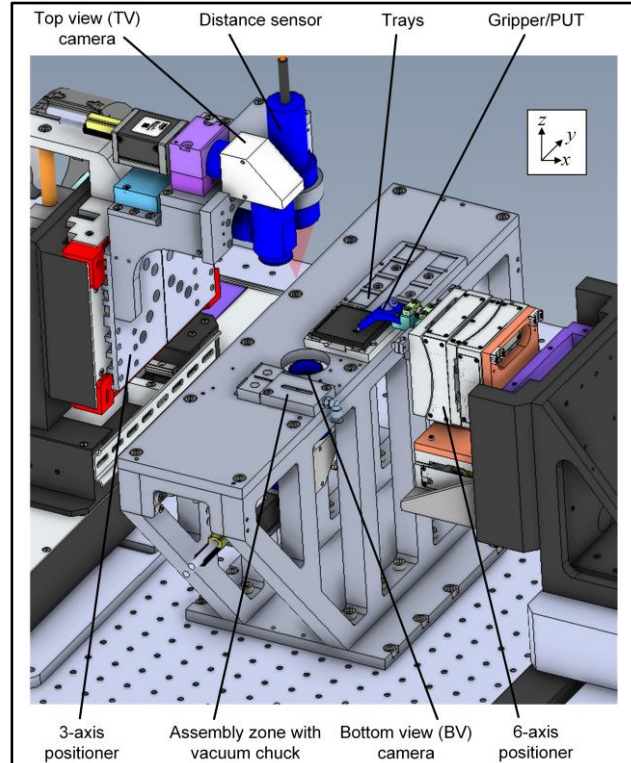
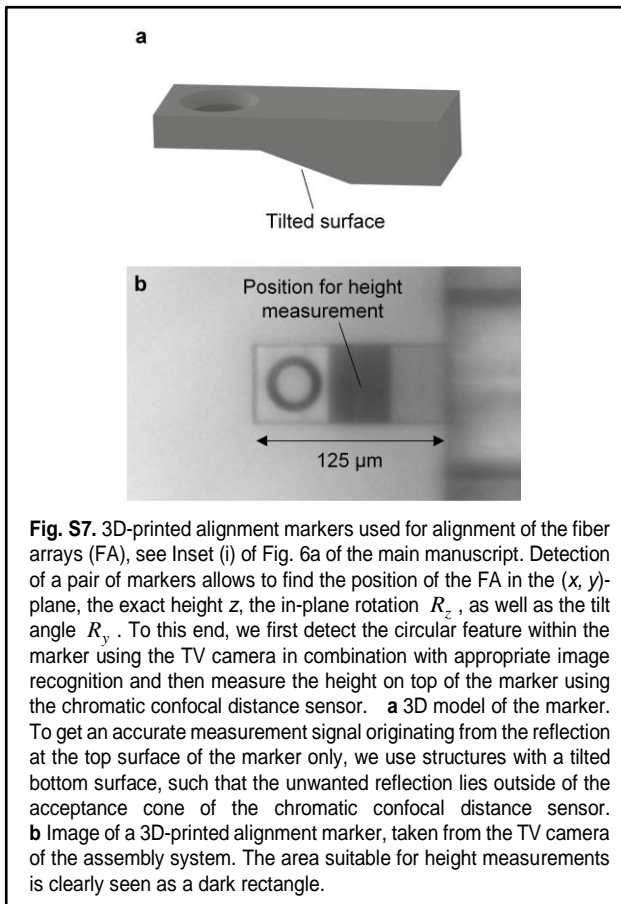


Fig. S6. Schematic of the assembly machine. The submount of the assembly is fixed at the assembly zone using a vacuum chuck. Components such as optical chips or fiber arrays are mounted using a six-axis positioner (right side) that is equipped with either a gripper or a vacuum pick-up-tool (PUT). The positions and orientations of components after pick-up and/or mounting are measured using a top-view (TV) camera and a chromatic confocal distance sensor², both mounted on a three-axis positioner (left side), as well as another fixed bottom-view (BV) camera. In a typical assembly workflow, parts are first picked up from the tray, inspected over the BV camera if necessary, and moved over to the assembly zone for final alignment and fixing. The results of passive alignment processes can be benchmarked by using active alignment techniques, which can also be executed on the assembly machine.

array (PDA). As a reference, the result of this passive alignment is then compared to an active alignment obtained by maximizing the output current of the photodiodes, which are contacted through an additional pair of DC-probes (not shown in Fig. S6).

In our experiments, we first glue the chips to the submount and then align the FA with respect to the chips, where the fibers are typically oriented along the y -direction, see Fig. S6, for optimum strain relief. The position in the (x, y) -plane and the in-plane-rotation R_z of the mounted chips are measured using the TV camera, while the exact chip height z and the chip tilt angles R_x and R_y are measured using line scans with the chromatic confocal distance sensor. For the FA, we first measure the position and orientation after pick-up and then calculate the motion of the six-axis positioner that is required to move the FA to its target position. To this end, we first find the rotation angle R_x from a BV autofocus measurement at the front and back of the FA. All other degrees of freedom of the FA within the gripper are then measured with the help of 3D-printed markers, see Fig. S7, which are

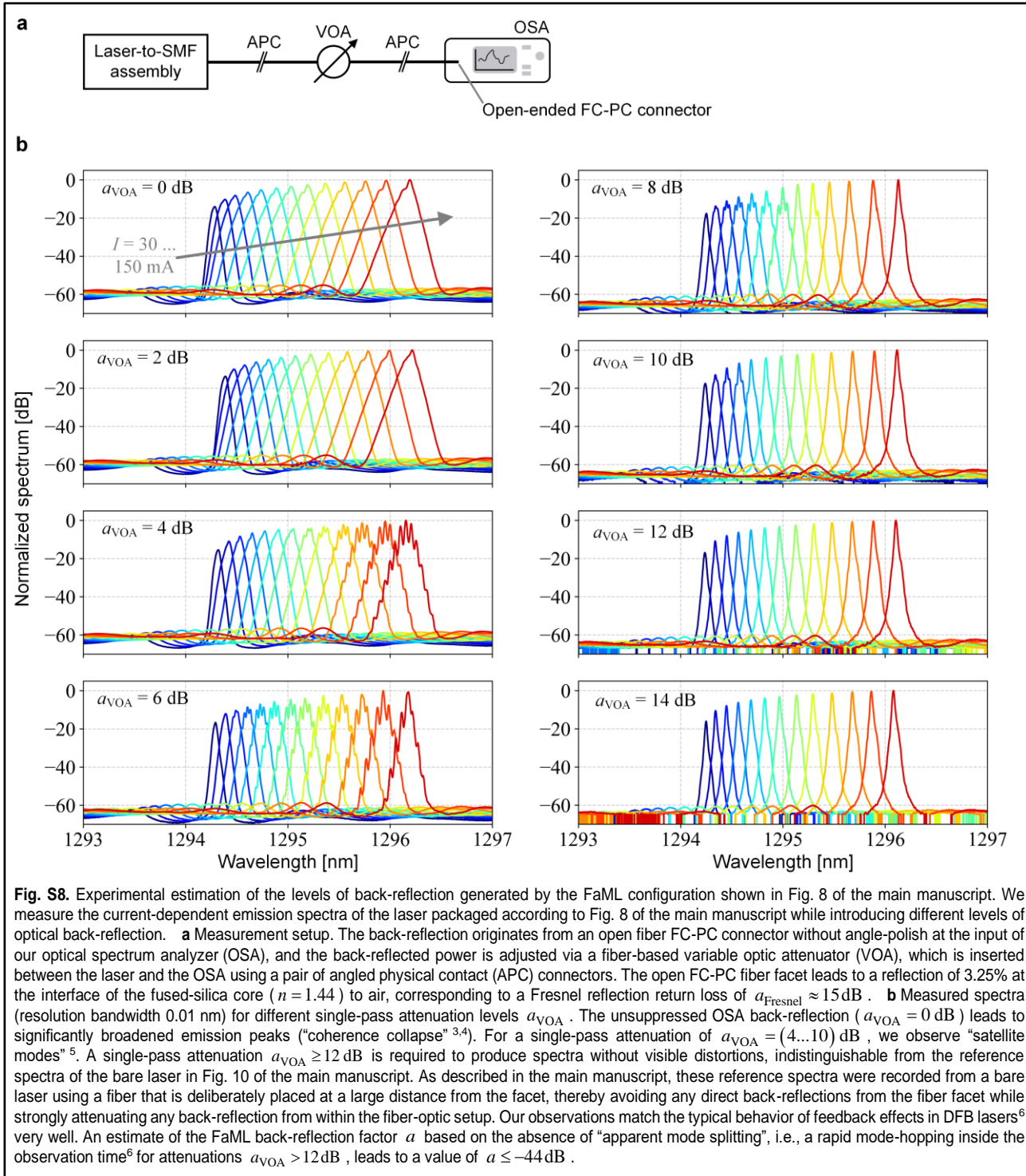


precisely aligned to unused channels of the FA during lithography. Specifically, we find the position in the (x, y) -plane and the in-plane rotation R_z by detecting the circular shapes within the markers using the TV camera in combination with appropriate image recognition techniques. The tilt angle R_y as well as the exact height z of the FA are found by height measurements on top of the 3D-printed markers using the chromatic confocal distance sensor. To get an accurate measurement signal originating from the reflection at the top surface of the marker only, we use structures with an angled bottom surface, such that the unwanted reflection lies outside of the acceptance cone of the chromatic confocal distance sensor.

4. Estimation of return loss induced by FaML-assemblies for angled facets

In our third set of experiments, see Section “Coupling to device arrays with angled facets” of the main manuscript, we demonstrate the viability of a special FaML configuration with low back-reflection. Such configurations allow, e.g., for coupling of arrays of reflection-sensitive angled-facet lasers to fiber arrays or to other PIC. In our experiments, we do not find any signs of detrimental effects that could be attributed to our packaging concept. However, the exact back-reflection factor induced by the FaML is hard to quantify by a direct measurement, and we thus perform an estimate of the expected levels of back-reflection. To this end, we measure

the current-dependent emission spectra of the laser packaged according to Fig. 8 of the main manuscript while varying the level of optical back-reflection. This back-reflection is generated by an open fiber FC-PC connector without angle-polish at the input of our optical spectrum analyzer, see Fig. S8a, and the back-reflected power is adjusted via a fiber-based variable optic attenuator (VOA), which is inserted between the laser and the OSA. The open fiber end leads to a reflection of approximately 3.25 % ($n = 1.44$ to air), corresponding to a Fresnel reflection return loss of $a_{\text{Fresnel}} \approx 15$ dB. We record spectra for various levels of single-pass attenuation a_{VOA} of the VOA, Fig. S8b. All spectra are recorded from DFB #2 of our assembly, with a single-pass coupling loss $a_{\text{FaML}} = 2.5$ dB of the FaML-pair, see Table 3 of the main manuscript. An unsuppressed OSA back-reflection ($a_{\text{VOA}} = 0$ dB) leads to significant broadened emission peaks (“coherence collapse”^{3,4}). For a single-pass attenuation of $a_{\text{VOA}} = (4 \dots 10)$ dB, we observe “satellite modes”⁵ with a separation corresponding to the relaxation oscillation frequency. A single-pass attenuation $a_{\text{VOA}} \geq 12$ dB is required to produce spectra without visible distortions, indistinguishable from the reference spectra of the bare laser in Fig. 10 of the main manuscript. As described in the main manuscript, these reference spectra were recorded from a bare laser using a fiber that is deliberately placed at a large distance from the facet, thereby avoiding any direct back-reflections from the fiber facet while strongly attenuating any back-reflection from within the fiber-optic setup. Our observations match the typical behavior for feedback effects in DFB lasers according to Tkach and Chraplyvy⁶ very well. There, the transition from satellite modes to a single narrow line (“Regime IV” to “Regime III” in Reference⁶) is found at an approximate threshold back-reflection factor of $a = -40$ dB, independent on the distance of the reflection, as long as the distance remains within the coherence length of the laser. We find this transition at $a_{\text{VOA}} = 10$ dB, and hence the very same threshold back-reflection factor, $a = -(2a_{\text{FaML}} + 2a_{\text{VOA}} + a_{\text{Fresnel}}) = -40$ dB. Two more transitions are usually found at even weaker back-reflections. In particular, a further transition (“Regime III” to “Regime II” in Reference⁶) is usually found at a distance-independent back-reflection factor of approximately $a = -45$ dB, where the laser would start to show an “apparent splitting” of the emission line, arising from rapid mode hopping⁶. In our experiments, we do not observe this effect when increasing the attenuations to $a_{\text{VOA}} > 12$ dB. We attribute this observation to the fact that the FaML introduces a slight amount of back-reflection as well, which can lead to an operation regime in which the laser emits a single narrow line while being only sensitive to other reflections of comparable or greater magnitude (“Regime III”, between -40 dB and -45 dB in Reference⁶). Since $a_{\text{VOA}} \geq 12$ dB is required to produce unperturbed spectra, we may further assume that the strength of the back-reflection from the FaML is approximately comparable to or smaller than the strength of the external back-reflection from the open fiber end for

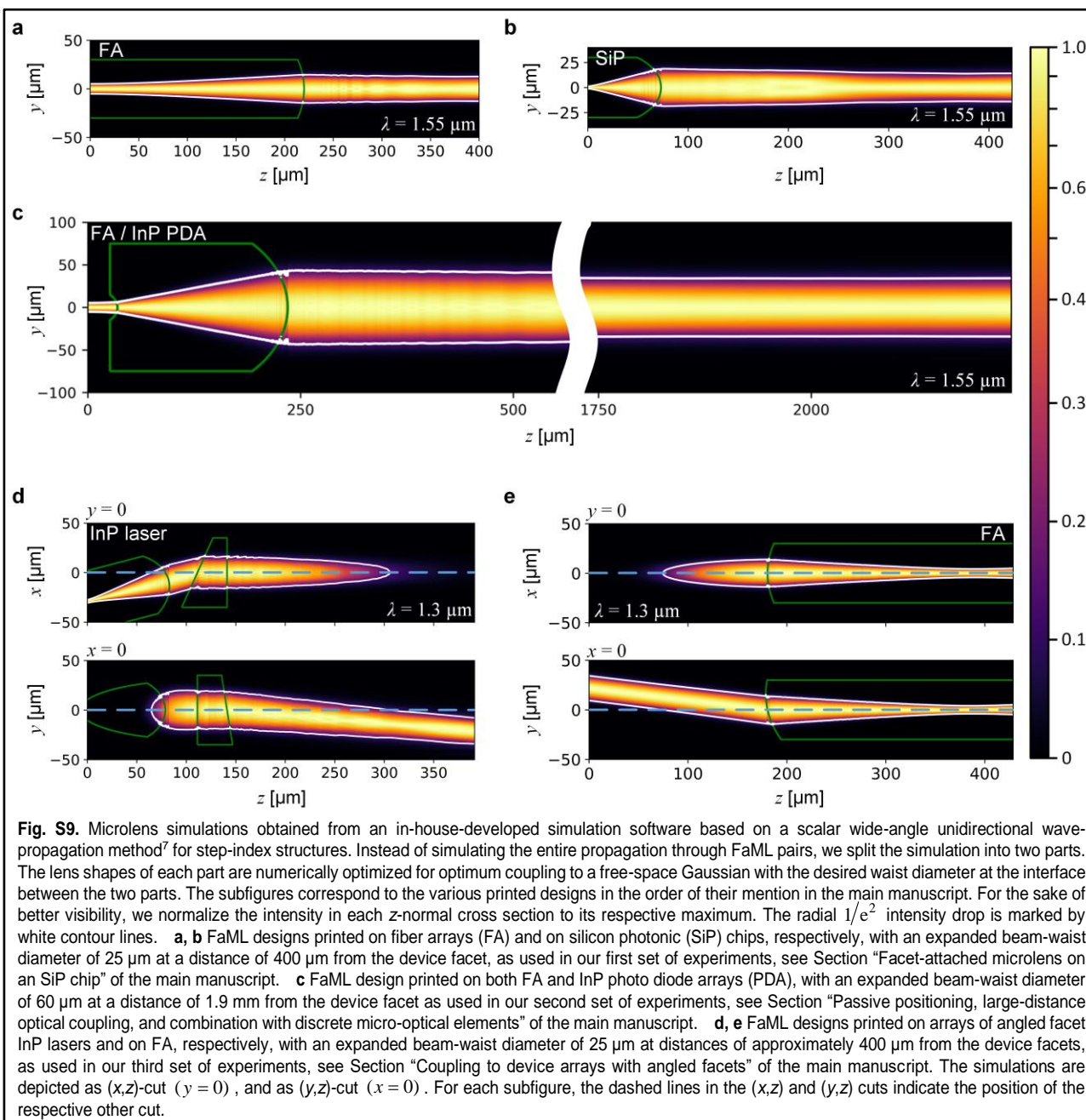


$$a_{\text{VOA}} = 12 \text{ dB}, \quad \text{which amounts to } -(2a_{\text{FaML}} + 2a_{\text{VOA}} + a_{\text{Fresnel}}) = -44 \text{ dB}.$$

5. Microlens simulations

For simulation of the microlenses, we use an in-house developed simulation software based on the scalar wide-angle unidirectional wave-propagation method for step-index structures proposed in Ref⁷, see Materials and Methods

section of the main manuscript. Instead of simulating the entire propagation through FaML pairs, we split the simulation into two parts, each containing one FaML. The shape of each of the two FaML is then numerically optimized for optimum coupling to a Gaussian mode field in free-space with the desired mode-field diameter. Figure S9 shows the simulated intensity distributions of all printed lens designs, in the order of their mention in the main manuscript. For the sake of better visibility, we normalize the intensity in each z -normal



cross section to its respective maximum. The radial $1/e^2$ intensity drop is marked by white contour lines.

For the lenses in our first and second set of experiments, Fig. S9a-c, we use a rotational symmetric even-order polynomial representation of the lens surface height,

$$h(r) = c_0 + c_2 r^2 + c_4 r^4 + \dots, \quad (\text{S29})$$

where $r = \sqrt{x^2 + y^2}$. The two-surface FaML beam expander, see Fig. S9c, produces an expanded MFD of $60\ \mu\text{m}$ and has a correspondingly large second lens surface. Due to the scaling laws of aberrations^{8,9} we therefore used a maximum of five free parameters c_0, c_2, c_4, c_6 and c_8 for this second surface, whereas all other surfaces required a lesser number of parameters.

For our third set of experiments, we use a more sophisticated parametrization of the lens surfaces. For the FaML on angled facet InP lasers, Fig. S9d, we assume a slightly elliptical spot of $3.2\ \mu\text{m} \times 2.2\ \mu\text{m}$ emitted from the laser facet, as measured using an infrared microscope equipped with a $100\times/0.8$ objective in air. To transform the elliptic beam into a beam with a circular cross section, we use a non-rotational symmetric parametrization based on conic sections¹⁰,

$$h(x, y) = h_0 + \frac{x^2 \rho_x + y^2 \rho_y}{1 + \sqrt{1 - (1 + K_x)(x \rho_x)^2 - (1 + K_y)(y \rho_y)^2}}, \quad (\text{S30})$$

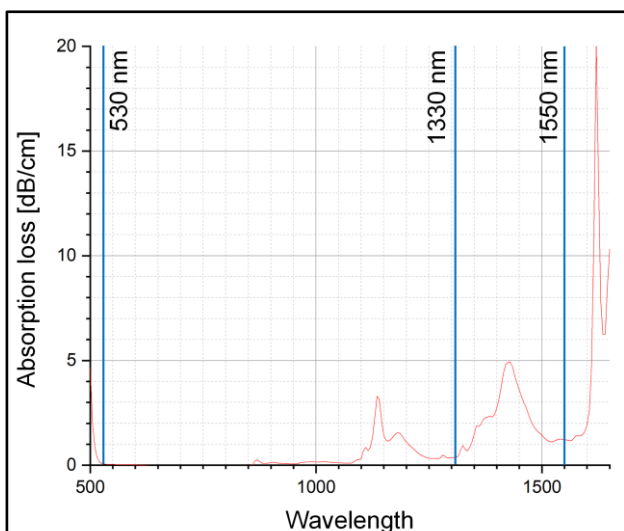


Fig. S10. Absorption spectrum of VanCore B (Vanguard Automation GmbH, Karlsruhe, Germany), which is similar to the resist VanCore A used for the FaML presented in the main manuscript. The vertical lines indicate wavelengths for typical applications around 530 nm, 1330 nm, and 1550 nm. For typical lengths of microlenses, the absorption loss is negligible. Specifically, in the wavelength range around 1550 nm, a typical absorption of 1 dB/cm leads to a loss of approximately 0.03 dB for a 300 μm interaction length of the light and the bulk material.

where ρ_x and ρ_y are the curvatures, i.e., the reciprocal values of the curvature radii in the apex, in the cut-plane containing the x -axis ($y = 0$), respectively in the cut-plane containing the y -axis ($x = 0$), and where K_x and K_y denote the conic constants in the respective cut-plane. A value of $K > 0$ corresponds to an oblate elliptical cross-section, $K = 0$ corresponds to a spherical cross-section, a value $-1 < K < 0$ corresponds to a prolate elliptical cross-section, $K = -1$ to a parabolic one, and $K < -1$ to a hyperbolic one. For optimization of the lens surface, we vary the parameters ρ_x , ρ_y , K_x , and K_y for best coupling efficiency to a Gaussian beam with the targeted mode-field diameter. Note that a single lens surface is generally insufficient to transform a diverging beam with an elliptic cross section into a collimated beam with a circular cross section and a pre-defined beam diameter. The beam profile generated by the optimized lens surface according to Eq. (S30) is hence subject to a slight residual ellipticity and astigmatism. The simulated impact on the coupling efficiency, however, is rather small (< 0.2 dB) and can hence be tolerated.

6. Transparency and stability of printed structures

FaML-based photonic systems can be utilized for a wide variety of applications, spanning a broad range of wavelengths. Hence, the wavelength-dependent absorption of printed structures is an important characteristic. Figure S10 shows an absorption spectrum of the photoresist VanCore B (Vanguard Automation GmbH, Karlsruhe, Germany), which is very similar to VanCore A as used for the structures in the main manuscript. The vertical blue lines indicate wavelengths for typical applications around 530 nm, 1330 nm, and

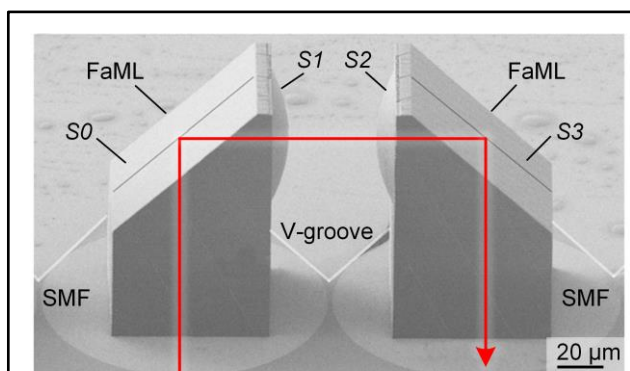


Fig. S11. Scanning electron microscopy (SEM) image of a simplified test structure for evaluating the long-term stability of 3D-printed facet-attached microlenses (FaML). The test vehicle consists of a pair of single-mode fibers (SMF) glued into V-grooves. Each of the SMF facets carries a 3D-printed FaML, designed as a loopback: Light coupled into the left SMF enters the first FaML, is redirected by total-internal-reflection (TIR) at the mirror with Surface S0 and collimated by the lens Surface S1. The beam then enters the second FaML through the lens Surface S2, is redirected by a second TIR mirror with Surface S3, and is finally coupled into the core of the right SMF. The path of the signal is indicated by the red arrow. The line in the center of the TIR mirrors has been added for a better orientation. Note that the SEM image, which was taken from a test structure after exposure to 85°C and 85% relative humidity for nearly 4000 h, does not show any sign of degradation.

1550 nm. Note that the typical interaction length of light with the bulk FaML material is below 300 μm such that absorption losses on a dB/cm level are usually negligible. Specifically, in the wavelength range around 1550 nm, a typical absorption of 1 dB/cm leads to a loss of approximately 0.03 dB for a lens with a length of 300 μm .

For industrial applications, the mechanical stability of the FaML are of great interest. Due to the small volume of the FaML, the adhesive forces are particularly strong relative to the mass, and the structures are hence very stable with respect to accelerations and vibrations – even under the stringent requirements set forth in Telcordia protocols^{11,12} GR-468-CORE/GR-1221-CORE, with random vibrations and accelerations up to 500 g. Still, FaML are rather sensitive to mechanical damage by direct physical contact, which should be avoided by appropriate handling procedures – just like for any optical facet of a PIC.

Finally, long-term and temperature stability of 3D-printed FaML is a key aspect with respect to practical application of the concept. The long-term stability of printed dielectric waveguides (photonic wire bonds, PWB) has previously been demonstrated in Ref¹³. More recently, similar investigations were done for FaML. In these experiments, we monitor the evolution of the coupling loss under pertinent damp-heat test conditions. We use a simplified test structure, see Fig. S11, store it in a climate chamber at 85°C and 85% relative humidity, and repeatedly measure the optical transmission at a wavelength of $\lambda = 1550$ nm over the course of nearly 4000 hours. The assembly consists of a pair of single mode fibers (SMF) glued into V-grooves. Each of the SMF facets carries a 3D-printed FaML, designed as a loopback: Light

coupled into the left SMF enters the first FaML, is redirected by total-internal-reflection (TIR) at the mirror with Surface S0, collimated by the lens Surface S1, and collected by a symmetrically arranged counterpiece, see red beam path in Fig. S11. The FaML consisted of the photoresist VanCore B (Vanguard Automation GmbH, Karlsruhe, Germany).

Table S1. Long-term stability tests of FaML at a temperature of 85°C and at a relative humidity of 85%

Connection	Coupling loss [dB]			
	Initial	400 h @ 85°C/85%	1840 h @ 85°C/85%	3960 h @ 85°C/85%
#1	1.4	1.4	1.5	1.3
#2	1.2	1.2	1.3	1.4
#3	1.5	1.6	1.9	1.5
#4	1.4	1.6	1.8	1.5
#5	1.5	1.6	1.5	1.5

We measured the transmission through five identical arrangements as in Fig. S11. The results of these long-term stability tests are shown in Table S1. Within our measurement accuracy, we did not find any sign of degradation for any of the five measured assemblies. The test had to be stopped after 3960 hours, because the single-mode connectors and the coating of the fibers had deteriorated under the harsh testing conditions to the extent that further reliable measurements were impossible. The FaML themselves did not show any visible degradation, see Fig. S11. In a further set of experiments, we investigated the stability of FaML similar to the ones shown in Fig. S11 at standard reflow-soldering temperatures of up to 260°C for several minutes. We did not observe any degradation of the measured transmission performance in these experiments.

Acknowledgements

This work was supported by the Deutsche Forschungsgemeinschaft (DFG, German Research Foundation) under Germany's Excellence Strategy via the Excellence Cluster 3D Matter Made to Order (EXC-2082/1-390761711) and the Collaborative Research Center WavePhenomena (CRC 1173), by the Bundesministerium für Bildung und Forschung (BMBF) via the projects PRIMA (# 13N14630), DiFeMiS (# 16ES0948), which is part of the programme "Forschungslabore Mikroelektronik Deutschland (ForLab), and Open6GHub (# 16KISK010), by the European Research Council (ERC Consolidator Grant 'TeraSHAPE'; # 773248), by the H2020 Photonic Packaging Pilot Line PIXAPP (# 731954), by the Alfried Krupp von Bohlen und Halbach Foundation, and by the Karlsruhe School of Optics and Photonics (KSOP).

Author contributions

The approaches and experiments were conceived by Y.X., P.Ma., M.T., P.-I. D., M.B., and C.K.. The authors M.B. and Y.X. developed the advanced microlens design tools and the lithography tools required for the precise fabrication of microlenses at device facets. Y.X. designed the microlenses. The demonstrators were built by Y.X. with the help of P.Ma.. P.-I. D. developed the photoresist used in the experiments. A.W. and C.D. designed and implemented

the assembly machine. Y.X., P.Ma., M.T., and T.K. developed the assembly processes. Y.X. performed the experimental characterization of the various assemblies with the help of P.Ma. and analyzed the measurement data. R.J. assisted with the process development for lenses at the facets of SiP chips. P.Mo. and K.G. contributed to the LEGO demonstrator. J.S. and A.S. contributed the InP photodiodes, and B.K. the InP lasers. The layout of the SiP chip was done by A.A.. All authors discussed the data. Y.X., W.F. and C.K. wrote the manuscript. The project was supervised by W.F., P.O.B., and C.K..

Data availability

The data that support the plots within this paper and other findings of this study are available from the corresponding author upon reasonable request.

Conflict of interest

P.-I.D. and C.K. are co-founders and shareholders of Vanguard Photonics GmbH and Vanguard Automation GmbH, start-up companies engaged in exploiting 3D nanoprinting in the field of photonic integration and assembly. A.W. is an employee of ficonTEC Service GmbH, a company selling assembly machines, and a former employee of Vanguard Automation GmbH. Y.X., P.Ma., M.B., M.T., P.-I.D., and C.K. are co-inventors of patents owned by Karlsruhe Institute of Technology (KIT) in the technical field of the publication. M.B. and M.T. are now employees of Nanoscribe GmbH, a company selling 3D lithography systems. T.K. and C.D. are employees of ficonTEC Service GmbH. The remaining authors R.J., J.S., A.S., A.A., B.K., P.M., K.G, P.O. and W.F. declare no competing interests.

References

- Joyce, W. B. & DeLoach, B. C. Alignment of Gaussian beams. *Appl. Opt.* **23**, 4187–4196 (1984).
- Precitec GmbH & Co. KG. Chromatic confocal technology. Available online: <https://www.precitec.com/optical-3d-metrology/technology/chromatic-confocal-sensors/>.
- Lenstra, D., Verbeek, B. & Den Boef, A. Coherence collapse in single-mode semiconductor lasers due to optical feedback. *IEEE J. Quantum Electron.* **21**, 674–679 (1985).
- Henry, C. & Kazarinov, R. Instability of semiconductor lasers due to optical feedback from distant reflectors. *IEEE J. Quantum Electron.* **22**, 294–301 (1986).
- Miles, R. O., Dandridge, A., Tveten, A. B., Taylor, H. F. & Giallorenzi, T. G. Feedback-induced line broadening in cw channel-substrate planar laser diodes. *Appl. Phys. Lett.* **37**, 990–992 (1980).
- Tkach, R. & Chraplyvy, A. Regimes of feedback effects in 1.5- μm distributed feedback lasers. *J. Lightw. Technol.* **4**, 1655–1661 (1986).
- Schmidt, S. *et al.* Wave-optical modeling beyond the thin-element-approximation. *Opt. Express* **24**, 30188 (2016).
- Lohmann, A. W. Scaling laws for lens systems. *Appl. Opt.* **28**, 4996–4998 (1989).
- Brady, D. J. & Hagen, N. Multiscale lens design. *Opt. Express* **17**, 10659–10674 (2009).
- Schuhmann, R. Description of aspheric surfaces: *Adv. Opt. Technol.* **8**, 267–278 (2019).
- Telcordia. GR-468-CORE: Reliability assurance for optoelectronic devices. (2004). Available online: <https://telecom-info.telcordia.com/site-cgi/ido/docs.cgi?ID=SEARCH&DOCUMENT=GR-468>.
- Telcordia. GR-1221-CORE: Generic Reliability Assurance Requirements for Passive Optical Components. (2010). Available online: <https://telecom-info.njdepot.ericsson.net/site-cgi/ido/docs.cgi?ID=SEARCH&DOCUMENT=GR-1221>.
- Blaicher, M. *et al.* Hybrid multi-chip assembly of optical communication engines by in situ 3D nano-lithography. *Light Sci. Appl.* **9**, 71 (2020).